ChemComm

COMMUNICATION

View Article Online
View Journal | View Issue

Cite this: *Chem. Commun.*, 2025, **61**, 19269

Received 9th May 2025,
Accepted 27th October 2025

DOI: 10.1039/d5cc02552d

rsc.li/chemcomm

Bulk photocatalysis within anatase-TiO_2–SiO_2 monoliths for efficient VOC photodegradation

Elodie Layan,[ab] Guillaume Clermont,[a] Isabelle Ly,[b] Frédéric Nallet,[b] Renaud A. L. Vallée,[b] Thierry Pigot,[c] Rénal Backov,[b] Mickael Le Bechec *[c] and Thierry Toupance *[a]

Self-standing anatase-TiO_2–SiO_2 composites bearing multiscale porous architecture demonstrated improved performance in the photodegradation of volatile organic compounds, achieving 80% propan-2-one mineralisation at a Ti/Si molar ratio as low as 0.08–0.15. These properties are related to the materials' unique 'meta-leaf' behaviour, enabling bulk photocatalysis by acting as a 'photonic sponge'.

In the broad context of global energy transition and environmental remediation, semiconductor-based heterogeneous photocatalysis is considered a key technology for achieving sustainable growth and development.[1,2] For instance, the environmental purification of contaminated air through the photocatalytic oxidation of volatile organic compounds (VOCs) in the gas phase appears to be very promising.[3] In this field, titanium dioxide (TiO_2) is the best-understood metal–oxide photocatalyst prototype owing to various basic and practical features such as low cost, nontoxicity, and high biological, chemical and photochemical stability along with good photocatalytic efficiency.[4] However, TiO_2 shows some limitations due to its weak solar light harvesting ability, the fast recombination of photogenerated electron–hole pairs, weak conductivity leading to poor electron–hole separation, and inherently slow reaction kinetics. To circumvent these drawbacks, many strategies have been developed either to improve solar light harvesting *via* doping approaches[5] or to enhance charge separation through combining TiO_2 with metal,[6] p-type[7] or n-type metal oxide[8] particles. More recently, the key role of photocatalyst geometry has been evidenced in the field of gas-phase photocatalysis.[9] In this context, our group has proposed an innovative concept to increase the volume/surface ratio effectiveness of photoactive materials by exploiting the light-trapping, *i.e.* photonic, properties of silica-based monoliths showing multiscale organization and hierarchical porosity, in combination with commercial P25 TiO_2 particles. These monoliths are fractal in nature and can be seen as tightly crumpled sheets of paper, leaving a lot of surface area accessible within the bulk. They can be named 'meta-leaves'. These 'meta-leaves' are SiO_2 walls containing TiO_2 catalyst particles, which can be easily accessed through photonic diffusion and therefore act as 'photonic sponges'. Thus, P25-TiO_2–SiO_2 monoliths showed excellent photocatalytic properties both regarding solar fuel production[10] and VOC photoabatement,[11] while optimizing photon efficiency as much as possible.[12] Nonetheless, P25, a mixture of 80% anatase and 20% rutile TiO_2 polymorphs, exhibits rather average textural properties. This would warrant investigating TiO_2 materials with better textural properties, such as anatase TiO_2 nanoparticles.

Herein, we report a new class of self-standing TiO_2–SiO_2 composites, including pure anatase TiO_2 nanoparticles, prepared by a sol–gel process, which showed enhanced photocatalytic properties for the gas-phase decomposition of propan-2-one.[13] In particular, it turns out that the unique photonic properties of these composites enable a significant decrease in the amount of TiO_2 powder used while keeping photomineralization rates high.

Anatase TiO_2–SiO_2 self-standing monoliths, hereafter named MUB-300(x), where x stands for the nominal Ti/Si molar ratio (x = 0.025, 0.05, 0.08, 0.15, 0.25, or 0.4) (Table S1), were prepared according to a previously reported procedure[11] using anatase TiO_2 nanoparticles[14] instead of P25 particles. As expected, ICP analyses revealed an increase in Ti loading as the amount of TiO_2 powder used increased (Table S2).

Regardless of the anatase TiO_2 content, the MUB-300(x) series shows a monolithic nature (Fig. 1A and B), where loose powder is no longer present. SEM images reveal the formation of aggregated hollow silica spheres arising from the departure of oil droplets from the starting direct emulsion, leading to macropores (Fig. 1C–K). Moreover, the silica walls exhibit connecting apertures stemming from the partial coalescence of oil droplets, network shrinkage occurring during sol–gel polycondensation, and subsequent thermal treatment. The resulting opened macroporous morphology is typical of Si(HIPE)-based materials[15] and crucial for catalysis aimed at pollutant abatement applications. Interestingly, the amount of anatase TiO_2 does not affect the morphology on the macroscopic scale, in contrast to what has been reported for the

[a] *Univ. Bordeaux, CNRS, Bordeaux INP, ISM, UMR 5255, 351 Cours de la Libération, F-33405 Talence, Cédex, France. E-mail: thierry.toupance@u-bordeaux.fr*
[b] *Univ. Bordeaux, CNRS, Bordeaux INP, CRPP, UMR 5031, 33600 Pessac, Cédex, France*
[c] *Université de Pau et des Pays de l'Adour, E2S UPPA, CNRS, IMT Mines Alès, IPREM, 64000 Pau, France. E-mail: mickael.lebechec@univ-pau.fr*

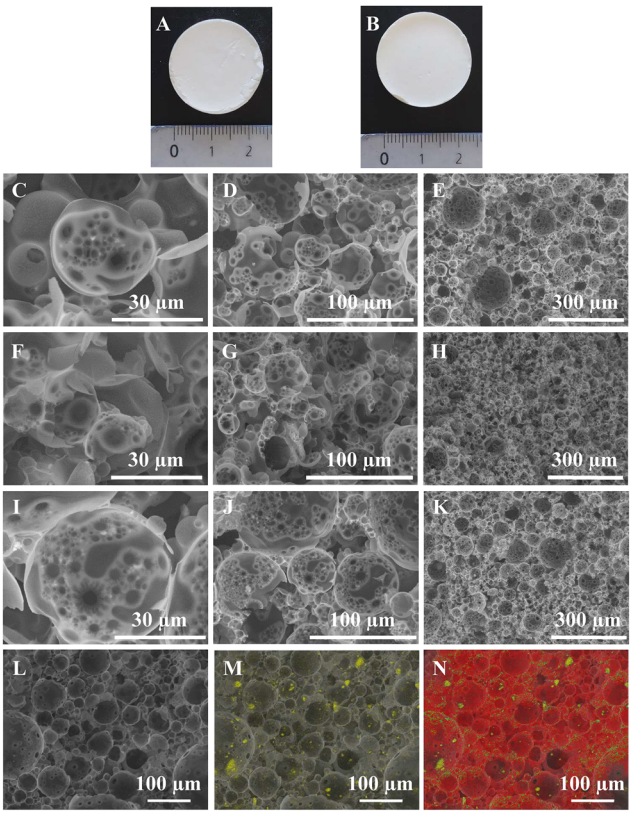

Fig. 1 A macroscopic view of the MUB-300 series: images of the self-standing monoliths MUB-300(0.08) (A) and MUB-300(0.25) (B). SEM images of MUB-300(0.05) (C–E), MUB-300(0.15) (F-H) and MUB-300(0.4) (I–K); and SEM images and EDX mapping of MUB-300(0.40) showing Ti (yellow) and Si (red) (L–N).

MUB-200(x) series including P25 particles.[11] In addition, EDX mapping performed on MUB-300(0.4) shows a homogeneous dispersion of anatase TiO_2 particles in the form of aggregates throughout the siliceous matrix (Fig. 1L–N). The macroporosity was further assessed through mercury intrusion porosimetry (Fig. S3). The pore sizes— that is, the junction windows hindering mercury imbibition—were found to range between 1 and 10 μm for MUB-300(0.05), MUB-300(0.15) and MUB-300(0.4). In addition, the size distributions of the junction apertures do not vary significantly as a function of the anatase TiO_2 loading, signifying that the TiO_2 nanoparticles are rather weakly involved in oil/water interface stabilization, if involved at all.

The mesoscopic scale of MUB-300 materials was then probed by nitrogen sorption analysis and small-angle X-ray scattering (SAXS). Whatever the anatase TiO_2 content, the N_2 adsorption–desorption isotherms are typical of micro-mesoporous materials (Fig. S4A). First of all, the sorption isotherms show high gas uptake at low relative pressure, which is characteristic of the presence of micropores (<2 nm). Moreover, a hysteresis loop between the adsorption and desorption branches is observed on each isotherm, related to the capillary condensation of N_2 inside mesopores (2 nm < pore size < 50 nm); this hysteresis becomes more pronounced as the TiO_2 content increases. This additional mesoporosity can be attributed to the interstices of TiO_2 nanoparticle aggregates. Pore size distribution studies confirm that the MUB-300(x) series is micro-mesoporous (Fig. S4B). In addition, the BET specific surface areas were found to range from 700 to 1200 $m^2\ g^{-1}$ without a clear trend relating to the TiO_2 loading (Table S3). The lack of a clear-cut trend relating the specific surface area to the TiO_2 loading can be explained. If the interstices between the TiO_2 nanoparticles increase with the TiO_2 nanoparticle content, we should not forget that the material density increases too, and that the specific area is expressed in $m^2\ g^{-1}$. As such, at low TiO_2 loadings, the specific area is even higher than that of the SiO_2 matrix (because the increase in density has not yet balanced the additional surface area induced by the interstices), while it decreases significantly at the highest loading, *i.e.* MUB-300(0.4), where the higher native density completely balances the increased surface area due to TiO_2 nanoparticle interstices. It is also worth mentioning that the samples MUB-300(0.08) and MUB-300(0.25) exhibit high BET surface areas due to the presence of a large amount of small mesopores, as evidenced by the inflection at low relative pressures, *i.e.* $0.1 < P/P_0 < 0.2$, and the large BJH surface areas.

The mesoscopic void organization was then investigated by SAXS experiments on MUB-300(0.15) (Fig. S5). Modeling the initial decay of the scattered intensity using a power law, *i.e.* $I \propto q^{-\nu}$, yielded an exponent value ν of about −2.9, definitely less negative than the value $\nu = -4$ predicted by Porod's law.[16] The standard value is associated with locally planar, randomly oriented interfaces; therefore, this suggests increased interfacial roughness compared to siliceous hierarchical porous self-standing monoliths.[17] For MUB-300(0.15), this is attributed to the presence of anatase TiO_2 nanoparticles randomly spread on the surface of the silica macropores. The Kratky representation of the same data ($I(q)xq^2$ as a function of q) emphasizes three peaks at $q \approx 0.09$, 0.16 and 0.18 $Å^{-1}$, as well as a smaller and broader feature at ~0.23 $Å^{-1}$. As detailed in the SI, these peaks can be related to the imprints left on the SiO_2 walls by the concentrated vermicular micellar phase employed for MUB-300 synthesis.

At the microscopic length scale, the crystalline structure of MUB-300 was investigated by powder XRD (Fig. S6). Regardless of the TiO_2 content, the XRD patterns showed features typical of the pure anatase polymorph. No trace of the rutile phase was detected even after thermal treatment at 700 °C, evidencing the high thermal stability of the anatase TiO_2-confined nanocrystals. As previously shown for MUB-200 including P25 nanoparticles,[11] the embedding of anatase particles within the silica matrix inhibits the anatase-to-rutile allotropic phase transition, even with thermal treatment up to 700 °C for 7 h. The average crystallite size was found to be 15.1 ± 0.4 nm for the pristine anatase particles and ranged between 14.2 and 14.8 ± 0.4 nm for MUB-300, which indicates no change in the crystallite size during MUB-300 processing and confirms the thermal stability of the anatase crystallites where Ostwald ripening is hampered.

The optical and light scattering properties of the MUB-300(x) series were investigated by diffuse reflectance UV-visible spectroscopy and by the photoreduction of a gold salt (Fig. 2). For each sample studied, the UV-visible diffuse reflectance spectrum shows a sharp edge at about 380 nm, as expected for TiO_2-based materials. Using Kubelka–Munk theory and postulating that anatase TiO_2 is

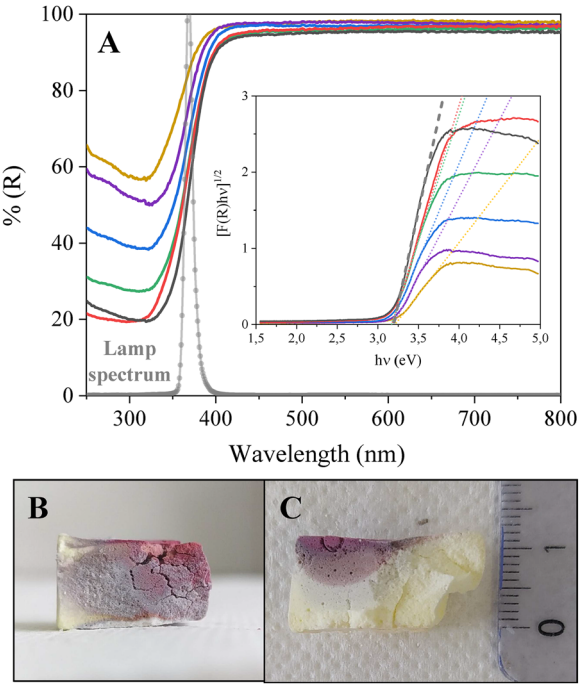

Fig. 2 Optical behaviour and photonic properties of the MUB-300 series. (A) UV-visible diffuse reflectance spectra and Kubelka–Munk plots ($[F(R) \times h\nu]^{1/2}$ as a function of $h\nu$ (eV)) (inset) for MUB-300(x) materials (x = 0.025: gold; x = 0.05: purple; x = 0.08: blue; x = 0.15: green; x = 0.25: red; and x = 0.40: black). (B and C) Images of MUB-300(0.025) and MUB-300(0.15) after impregnation with $KAuCl_4$ in propan-2-ol (0.01 M) followed by drying and further irradiation with a metal halide lamp (40 W cm^{-2}, emission spectrum shown in A) for 1 h.

an indirect band gap semiconductor,[18] the optical band gap of the MUB-300 series was estimated to be 3.2 eV, in agreement with that expected for pure anatase TiO_2 particles (Fig. 2A). Light penetration into the MUB-300 materials was then estimated by infiltrating a $KAu^{III}Cl_4$ salt solution within MUB-300 materials followed by UV-light illumination. A strong color change from pale yellow to red-purple, related to the plasmon absorption band of the Au^0 particles formed upon irradiation, was thus observed for MUB-300(0.025) and MUB-300(0.15) containing low and high amounts of anatase TiO_2, respectively. As indicated by the color of the monoliths (Fig. 2B and C), the light penetrates more than 1 cm and 6 mm for MUB-300(0.025) and MUB-300(0.15), respectively. This trend is consistent with an increase in anatase TiO_2 loading leading to more UV-light absorption and shallower light penetration depth. The MUB-300 series, therefore, behaves as a 'photonic sponge' and enables UV light to be diffused efficiently into the whole volume of the monoliths.

To evaluate the photocatalytic activity of the MUB-300 series, the photo-oxidation of propan-2-one as a model VOC was carried out in a batch reactor (Fig. S2) under UV illumination (LED: 365 nm, 2.7 mW cm^{-2}). After having checked that pure Si-HIPE led to no propan-2-one photodegradation (Fig. S7), propan-2-one (120 ppmV) was allowed to adsorb on the MUB-300(0.15) surface for 6 h, reaching a plateau value at 15 ppmV without the production of any CO_2 (Fig. 3A). As soon as UV illumination started, a strong increase in the CO_2 concentration, with a concomitant decrease in the propan-2-one concentration, was detected, reaching a plateau at about 300 ppmV after 16 h of irradiation. By postulating that the decomposition of 1 mole of propan-2-one can produce 3 moles of CO_2, the mineralization yield was estimated to be about 80%, evidencing the photodecomposition of most of the propan-2-one introduced into the reactor. To highlight the influence of the amount of anatase TiO_2 particles in the monoliths, the same experiments were carried out with the other MUB-300 materials. The mineralization yield increases from 55–60% for a Ti/Si molar ratio below 0.05 to reach a plateau value of 80–90% for a Ti/Si molar ratio between 0.08 and 0.25, followed by a slight decrease for a Ti/Si molar ratio around 0.4. Generally speaking, these mineralization rates are close to or even better than those reported for similar propan-2-one concentrations, *i.e.*, about 120 ppmV, with TiO_2 powder,[19] TiO_2 film[20] or TiO_2-supported on organic fibers.[21] To obtain deeper insights into the kinetic rates of the photodecomposition process, the apparent rate constant was determined for each MUB-300 sample studied. Whatever the Ti/Si molar ratio, the photodegradation of propan-2-one over the MUB-300 monoliths follows first-order laws: $\ln(C_0^{\text{propan-2-one}}/C^{\text{propan-2-one}}) = k_{\text{app}}^{\text{propan-2-one}} t$ and $\ln(100/100 - \%CO_2) = k_{\text{app}}^{CO_2} t$, where $k_{\text{app}}^{\text{propan-2-one}}$ and $k_{\text{app}}^{CO_2}$ are the pseudo-first-order rate constants for propan-2-one decomposition and CO_2 formation, respectively (Fig. 3B and Table S4). It is generally accepted that the propan-2-one degradation rate follows a simple Langmuir–Hinshelwood form,[22] which can be simplified at low pollutant concentrations to $\ln(C_0^{\text{propan-2-one}}/C^{\text{propan-2-one}}) = kK_{\text{ads}}t$, where k is the actual rate constant and K_{ads} is the propan-2-one adsorption constant on TiO_2.[23] The experimentally obtained linear correlation values are therefore fully consistent with this model and provide a quantitative estimation of the relative MUB-300 efficiency (Fig. 3B, see the SI for the experimental value of K_{ads}). It turns out

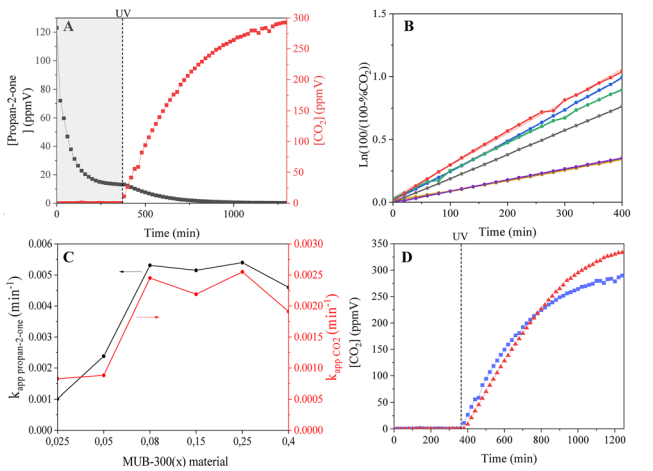

Fig. 3 Photocatalytic properties of the MUB-300 series. (A) The photo-oxidation of propa-2-one in the presence of MUB-300(0.15) with propa-2-one disappearance (black) and carbon dioxide formation (red) as a function of time (see the SI for experimental details). (B) Ln(100/(100 − %CO_2)) as a function of time for MUB-300(x) samples (x = 0.025: gold; x = 0.05: purple; x = 0.08: blue; x = 0.15: green; x = 0.25: red; and x = 0.40: black). (C) A comparison of the pseudo-first-order kinetic rate constants of propa-2-one decomposition and CO_2 formation for the MUB-300 series. (D) A comparison of the photocatalytic properties of MUB-300(0.15) (red triangles) and MUB-200(0.15) (blue squares) containing anatase TiO_2 and P25 TiO_2 particles, respectively.

that the apparent rate constants $k_{app}^{propan\text{-}2\text{-}one}$ and $k_{app}^{CO_2}$ increase rapidly upon increasing the Ti/Si molar ratio from 0 to 0.08 to reach a plateau value, *i.e.* 5.2–5.4 × 10^{-3} min^{-1} and 2.2–2.5 × 10^{-3} min^{-1} for $k_{app}^{propan\text{-}2\text{-}one}$ and $k_{app}^{CO_2}$, respectively, for Ti/Si molar ratios between 0.08 and 0.25. At higher Ti/Si molar ratios, the kinetic rate starts decreasing (Fig. 3C). Even though a comparison with literature data can hardly be made due to the wide diversity of experimental setups and photocatalytic conditions used, the $k_{app}^{CO_2}$ rate constants found for the MUB-300 series are in the same range as those reported for propan-2-one degradation with anatase TiO_2 powder, *i.e.* 0.34–7 × 10^{-3} min^{-1}.[23] In addition, compared to photocatalysts that have already been published, the MUB-300 series has the advantage of being a stable and efficient self-standing composite monolith, making it easier to handle, process, regenerate and reuse.

It is also worth mentioning that the MUB-300(x) series, including only anatase TiO_2 particles, showed comparable or even slightly higher photomineralization rates than the MUB-200(x) series, which contains reference P25 TiO_2 powder made of both rutile and anatase particles. The mineralization yield of propan-2-one reaches 85–90% for MUB-300(0.15) while MUB-200(0.15) leads to values of about 75–80% (Fig. 3D). This could be rationalized by considering that the anatase TiO_2 particles show a higher specific surface area, *i.e.* about 120 m^2 g^{-1}, than P25 particles, *i.e.* 45 m^2 g^{-1}, which counterbalances the better charge separation expected for P25 particles due to the heterojunction between rutile and anatase polymorphs. Furthermore, the use of anatase TiO_2 provides interesting findings about the influence of the TiO_2 loading on the photoactivity. First of all, the apparent kinetic rates follow the trend exhibited by the textural properties of MUB-300(x) (Fig. S8), indicating that the reactions are mediated by surface states accessible within the volume. In addition, theoretical considerations and calculations developed in the SI clearly show that the photocatalytic kinetic rates for propan-2-one degradation with the MUB-300(x) monoliths are governed by absorption-diffusion balance (Fig. S9). Thus, as the TiO_2 content increases, more UV photons are absorbed by the surface material, resulting in less UV light diffusing into the core of the material. Conversely, incident UV photons encounter more active sites in materials with a higher TiO_2 content. Therefore, for a Ti/Si molar ratio below 0.08, the mineralization yield increases with TiO_2 loading due to higher UV-light absorption arising from diffusion processes linked to the photonic structure of the monoliths. For Ti/Si molar ratios between 0.08 and 0.25, a plateau of photoactivity is reached due to a similar number of active sites being encountered, resulting from competition between diffusion phenomena, stemming from the photonic structure and absorption processes at the surface of the monoliths, which are richer in TiO_2 particles. Finally, the latter process becomes predominant for Ti/Si molar ratios greater than 0.4.

In summary, the MUB-300 series consists of self-standing anatase-TiO_2–SiO_2 composites exhibiting hierarchical micro-, meso- and macroporosity, open macroporosity and a very large surface area up to 1200 m^2 g^{-1}. These materials also behave as 'photonic sponges', where UV light can penetrate the bulk over several millimeters. This value is much higher than what is usually observed for conventional photocatalysts, such as particle beds, where light penetration is limited to the extreme surface, *i.e.* a few tens of microns. This unique 'meta-leaf' photonic behavior, acting in bulk, renders the MUB-300 series very efficient regarding the photodecomposition of volatile organic compounds (VOCs) such as propan-2-one, where footprint minimization and/or photoreactor miniaturization can become accessible, while avoiding the 2D cul-de-sac behavior observed in traditional heterogeneous photocatalysis. Moreover, the Ti/Si molar ratio can be decreased to 0.08–0.15, while maintaining mineralization yields around 80%.

This study received financial support from CNRS and the French government in the framework of the University of Bordeaux's IdEx "Investments for the Future" program/GPR PPM.

Conflicts of interest

There are no conflicts to declare.

Data availability

The data supporting this article have been included as part of the supplementary information (SI). Supplementary information is available. See DOI: https://doi.org/10.1039/d5cc02552d.

Notes and references

1 S. Lee, H.-S. Ba and W. Choi, *Acc. Chem. Res.*, 2023, **56**, 867.
2 H. Park, H.-I. Kim, G.-H. Moon and W. Choi, *Energy Environ. Sci.*, 2016, **9**, 411.
3 H. Sopha, M. Baudys, M. Sepulveda, J. Rusek, L. Hromadko, J. Rodriguez-Pereira, J. Krysa and J. M. Macak, *ACS Appl. Nano Mater.*, 2023, **6**, 17053.
4 Q. Guo, C. Zhou, Z. Ma, Z. Ren, H. Fan and X. Yang, *Chem. Soc. Rev.*, 2016, **45**, 3701.
5 C. Liu, Z. Liu and Y. Zhu, *Mater. Trans.*, 2018, **59**, 811.
6 Z. Hu, C. Yang, K. Lv, X. Li, Q. Li and J. Fan, *Chem. Commun.*, 2020, **56**, 1745.
7 J. Chen, M. Wang, J. Han and R. Guo, *J. Colloid Interface Sci.*, 2020, **562**, 313.
8 J. Mioduska, M. S. Lapinski, J. Karczewski, J. Hupka and A. Zielinska-Jurek, *Chem. Eng. Res. Des.*, 2023, **193**, 145.
9 F. Matter and M. Niederberger, *Adv. Sci.*, 2022, **9**, 2105363.
10 S. Bernadet, E. Tavernier, D.-M. Ta, R. A. Vallée, S. Ravaine, A. Fecant and R. Backov, *Adv. Func. Mater.*, 2019, **29**, 1807767.
11 E. Layan, J. Gupta, I. Ly, F. Nallet, A. Bentaleb, E. Laurichesse, R. Vallée, J.-L. Blin, B. Lebeau, F. Louërat, M. Le Bechec, P. Moonen, T. Toupance, T. Pigot and R. Backov, *Langmuir*, 2023, **39**, 3871.
12 J. Y. Y. Loh, A. Wang, A. Mohan, A. A. Tountas, A. M. Gouda, A. Tavasoli and G. A. Ozin, *Adv. Sci.*, 2024, **11**, 2306604.
13 M. L. Sauer and D. F. Ollis, *J. Catal.*, 1994, **149**, 81.
14 Z. Tebby, O. Babot, T. Toupance, D.-H. Park, G. Campet and M.-H. Delville, *Chem. Mater.*, 2008, **20**, 7260.
15 F. Carn, A. Colin, M.-F. Achard, H. Deleuze, E. Sellier, M. Birot and R. Backov, *J. Mater. Chem.*, 2004, **14**, 1370.
16 G. Porod, *General Theory in Small Angle X-ray Scattering*, Academic Press, New York, 1982, ch. 2, p. 17.
17 A. Vardon, M.-A. Dourges, E. Laurichesse, V. Schmitt, A. Bentaleb, F. Nallet, I. Ly and R. Backov, *Langmuir*, 2025, **41**, 26760.
18 Md. T. Uddin, Y. Nicolas, C. Olivier, T. Toupance, M. M. Müller, H.-J. Kleebe, K. Rachut, J. Ziegler, A. Klein and W. Jaegermann, *J. Phys. Chem. C*, 2013, **117**, 22098.
19 H. Liao, H. Xu, X. Zhang, W. Dai and Z. Zhang, *Appl. Catal., A*, 2023, **657**, 119158.
20 Y.-H. Li, S.-H. Yang, C.-S. Yuan, H. Shen and C.-H. Hung, *Aerosol Air Qual. Res.*, 2023, **23**, 220358.
21 G. Zhang, H. Wang, S. Guo, J. Wang and J. Liu, *Appl. Surf. Sci.*, 2016, **362**, 257.
22 M. Le Bechec, N. Kinadjian, D. Ollis, R. Backov and S. Lacombe, *Appl. Catal., B*, 2015, **179**, 78.
23 M. Bettoni, P. Candori, S. Falcinelli, F. Marmottini, S. Meniconi, C. Rol and G. V. Sebastiani, *J. Photochem. Photobiol. A: Chem.*, 2013, **268**, 1.

